Regular Article – Experimental Physics

Measurement of η photoproduction on the proton from threshold to 1500 MeV

The GRAAL Collaboration

O. Bartalini[2,9], V. Bellini[12,5], J.P. Bocquet[1], P. Calvat[1], M. Capogni[2,9,a], L. Casano[9], M. Castoldi[7], A. D'Angelo[2,9], J.-P. Didelez[14], R. Di Salvo[9], A. Fantini[2,9], D. Franco[2,9], C. Gaulard[4,b], G. Gervino[3,10], F. Ghio[8,11], G. Giardina[6,15], B. Girolami[8,11], A. Giusa[12,6], M. Guidal[14], E. Hourany[14], R. Kunne[14], A. Lapik[13], P. Levi Sandri[4], A. Lleres[1,c], F. Mammoliti[12,6], G. Mandaglio[6,15], D. Moricciani[9], A.N. Mushkarenkov[13], V. Nedorezov[13], L. Nicoletti[2,9,1], C. Perrin[1], C. Randieri[12,5], D. Rebreyend[1], F. Renard[1], N. Rudnev[13], T. Russew[1], G. Russo[12,6], C. Schaerf[2,9], M.-L. Sperduto[12,6], M.-C. Sutera[6], A. Turinge[13], and V. Vegna[2,9]

[1] LPSC, Université Joseph Fourier Grenoble 1, CNRS/IN2P3, Institut National Polytechnique de Grenoble, 53 avenue des Martyrs, 38026 Grenoble, France
[2] Dipartimento di Fisica, Università di Roma "Tor Vergata", via della Ricerca Scientifica 1, I-00133 Roma, Italy
[3] Dipartimento di Fisica Sperimentale, Università di Torino, via P. Giuria, I-00125 Torino, Italy
[4] INFN - Laboratori Nazionali di Frascati, via E. Fermi 40, I-00044 Frascati, Italy
[5] INFN - Laboratori Nazionali del Sud, via Santa Sofia 44, I-95123 Catania, Italy
[6] INFN - Sezione di Catania, via Santa Sofia 64, I-95123 Catania, Italy
[7] INFN - Sezione di Genova, via Dodecanneso 33, I-16146 Genova, Italy
[8] INFN - Sezione di Roma, piazzale Aldo Moro 2, I-00185 Roma, Italy
[9] INFN - Sezione di Roma "Tor Vergata", via della Ricerca Scientifica 1, I-00133 Roma, Italy
[10] INFN - Sezione di Torino, I-10125 Torino, Italy
[11] Istituto Superiore di Sanità, viale Regina Elena 299, I-00161 Roma, Italy
[12] Dipartimento di Fisica ed Astronomia, Università di Catania, via Santa Sofia 64, I-95123 Catania, Italy
[13] Institute for Nuclear Research, 117312 Moscow, Russia
[14] IPNO, Université Paris-Sud 11, CNRS/IN2P3, 15 rue Georges Clémenceau, 91406 Orsay, France
[15] Dipartimento di Fisica, Università di Messina, salita Sperone, I-98166 Messina, Italy

Abstract. Beam asymmetry and differential cross-section for the reaction $\gamma p \to \eta p$ were measured from production threshold to 1500 MeV photon laboratory energy. The two dominant neutral decay modes of the η-meson, $\eta \to 2\gamma$ and $\eta \to 3\pi^0$, were analyzed. The full set of measurements is in good agreement with previously published results. Our data were compared with three models. They all fit satisfactorily the results but their respective resonance contributions are quite different. The possible photoexcitation of a narrow state $N(1670)$ was investigated and no evidence was found.

PACS. 13.60.Le Meson production – 13.88.+e Polarization in interactions and scattering – 25.20.Lj Photoproduction reactions

1 Introduction

Eta photoproduction on the proton in the resonance region has been abundantly studied over the last years [1–9] and the initial expectation of a simple reaction mech-

anism has faded away. For the time being, apart from the well-established contributions of two resonances, the dominant $S_{11}(1535)$ and the $D_{13}(1520)$ whose excitation was clearly revealed by our beam asymmetry measurement close to threshold [2], the contribution of states in the third resonance region remains largely model-dependent [10–16]. Some models even need to incorporate new resonances [11,15].

Presently, the η photoproduction database contains mostly cross-section results and only a few single polariza-

[a] *Present affiliation*: ENEA - C.R. Casaccia, via Anguillarese 301, I-00060 Roma, Italy.
[b] *Present affiliation*: CSNSM, Université Paris-Sud 11, CNRS/IN2P3, 91405 Orsay, France.
[c] e-mail: lleres@lpsc.in2p3.fr

tion observable data. In addition to our beam asymmetry measurement, the target asymmetry was measured at the Bonn synchrotron up to 1100 MeV [3] and some preliminary beam asymmetries have been recently obtained by the CB-ELSA/TAPS Collaboration up to 1350 MeV [9]. Polarization observables, being sensitive to interference terms between different multipoles, bring valuable constraints on partial-wave analyses and therefore it is desirable to extend these measurements in the third resonance region.

In the present work, we report on precise measurements of the beam asymmetry Σ and of the differential cross-section for the reaction $\gamma p \rightarrow \eta p$ from production threshold ($E_\gamma = 707$ MeV) to 1500 MeV ($W = 1485$–1900 MeV). The extracted total cross-section is also presented. This work complements and improves our previously published results for energies up to 1100 MeV [2, 4].

Fig. 1. Schematic view of the LAγRANGE detector: BGO calorimeter (1), plastic scintillator barrel (2), cylindrical MW-PCs (3), target (4), plane MWPCs (5), double plastic-scintillator hodoscope (6), lead-scintillator shower detector (7) (the drawing is not to scale).

2 Experimental set-up

The experiment was carried-out with the GRAAL facility (see [17] for a detailed description and references therein), installed at the European Synchrotron Radiation Facility (ESRF) in Grenoble (France). The tagged and polarized γ-ray beam is produced by Compton scattering of laser photons off the 6.03 GeV electrons circulating in the storage ring.

In the present experiment, we used alternately the green line at 514 nm and a set of UV lines around 351 nm produced by an Ar laser, giving 1.1 and 1.5 GeV γ-ray maximum energies, respectively.

The photon energy is provided by an internal tagging system consisting of silicon microstrips (128 strips with a pitch of 300 μm) for measurements of the scattered electron position and a set of plastic scintillators for Time-of-Flight (ToF) measurements. The measured energy resolution of 16 MeV is dominated by the energy dispersion of the electron beam (14 MeV —all resolutions are given as FWHM). The energy calibration is extracted run by run from the fit of the Compton edge position with a precision of $\sim 10\,\mu$m[1], equivalent to $\Delta E_\gamma / E_\gamma \simeq 2 \times 10^{-4}$ (0.3 MeV at 1.5 GeV).

The energy dependence of the γ-ray beam polarization was determined using the Klein-Nishina formula and taking into account the laser and electron beam emittances. The γ-ray beam polarization is close to 100% at the maximum energy and decreases smoothly with energy down to a minimum of $\approx 30\%$ (UV) or $\approx 60\%$ (green) at the η production threshold. Based on detailed studies [17], it was found that the only significant source of error for the γ-ray polarization comes from the laser beam polarization ($\delta P_\gamma / P_\gamma = 2\%$).

A thin monitor is used to measure the beam flux (typically 10^6 γ/s). The monitor efficiency ($2.68 \pm 0.03\%$) was
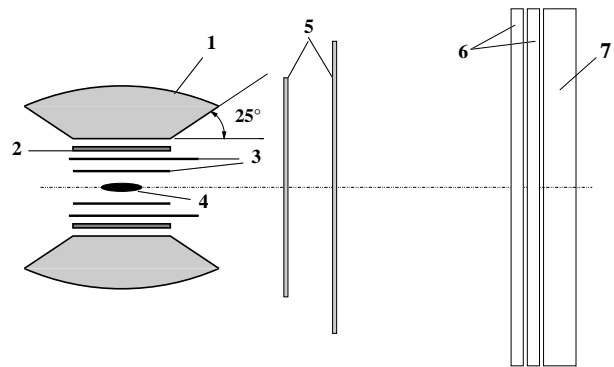
estimated by comparison with the response at low rate of a lead/scintillating fiber calorimeter.

The target cell consists of an aluminum hollow cylinder of 4 cm in diameter closed by thin mylar windows (100 μm) at both ends. The target (6 cm long for the present experiment) was filled by liquid hydrogen at 18 K ($\rho \approx 7 \; 10^{-2}$ g/cm^3).

The 4π LAγRANGE detector of the GRAAL set-up allows to detect both neutral and charged particles (fig. 1).

The γ-rays coming from the η neutral decay channels ($\eta \rightarrow 2\gamma$ and $\eta \rightarrow 3\pi^0 \rightarrow 6\gamma$— branching ratios of 39.2 and 32.2%, respectively) are detected in a BGO calorimeter made of 480 (15$\theta \times$ 32φ) crystals, each of 21 radiation lengths. They are identified as clusters of adjacent crystals (3 on average for an energy threshold of 10 MeV per crystal) with no associated hit in the barrel. The measured photon energy resolution is 3% on average. For a thin target (3 cm), the angular resolution is 6° and 7° for polar and azimuthal angles, respectively.

At forward angles, the γ-rays can be detected in a lead-scintillator sandwich ToF wall, consisting of 16 vertical modules. This detector provides a good angular resolution but no energy measurement and, for the present reaction, extends only marginally the covered angular range. For the sake of simplicity, it was not used in the present analysis.

The recoil proton track is measured by a set of Multi-Wire Proportional Chambers (MWPC) (see [19] for more details). Two cylindrical chambers with striped cathodes are used to cover the central region and give a reconstruction efficiency $\geq$ 90% with a resolution of 3.5° in θ and 4.5° in φ. The forward-angle tracks are measured by two planar chambers (efficiency $\geq$ 99%), each composed of two wire planes; the average polar and azimuthal resolutions are 1.5° and 2°, respectively.

Charged-particle identification in the central region is obtained by dE/dx technique thanks to a plastic scintillator barrel (32 bars, 5 mm thick, 43 cm long) with an energy resolution $\approx$ 20%. For the charged particles emitted in the forward direction, a ToF measurement is provided by a

---

[1] This high accuracy has allowed us to improve by three orders of magnitude the limit for the light speed anisotropy ($\Delta c / c \leq 3 \times 10^{-12}$) [18].

double plastic-scintillator hodoscope ($300 \times 300 \times 3\,\text{cm}^3$) placed at a distance of $3\,\text{m}$ from the target and having a resolution of $\approx 600\,\text{ps}$. This detector provides also a measure of the energy loss $\text{d}E/\text{d}x$. Energy calibrations were extracted from the analysis of the $\pi^0 p$ photoproduction reaction while the ToF calibration of the forward wall was obtained from fast electrons produced in the target.

For the cross-section measurements, due to large uncertainties on the cylindrical chambers efficiency, the proton direction was deduced from the association between the scintillator barrel and the BGO calorimeter at the cost of a worse resolution ($\sim 10°$ in θ and φ).

3 Data analysis

3.1 Channel selection

For the present results, the same selection method used in our previous publications on π^0 and η photoproduction [2,4,17,20] was applied. Only the main points will be recalled in the following.

The analysis method is based on two-body kinematics. Thanks to the complete detection of all final-state products, the kinematics of the reaction is overdetermined and a clean event selection can be achieved without the need for background subtraction.

Only events with two or six neutral clusters in the BGO calorimeter and a single charged-particle track were selected. Channel selection was achieved by applying cuts on the following quantities:

– $M_{2\gamma}$ or $M_{6\gamma}$,
– $R_\eta = E_\eta/E_\eta^*$,
– $\Delta\theta_p = \theta_p^* - \theta_p$,
– $\Delta\varphi_p = \varphi_p^* - \varphi_p$,
– $\Delta t_p = \text{ToF}_p^* - \text{ToF}_p$ (only at forward angles),

where the "*" indicates variables calculated from the two-body kinematics as opposed to measured ones. $M_{2\gamma}$ and $M_{6\gamma}$ are the invariant masses of the detected photons.

A Monte Carlo simulation of the apparatus based on the GEANT3 package, coupled with a complete event generator including all known photoproduction reactions [21], was used to optimize selection cuts, calculate detection efficiencies and estimate background contamination. To optimize event selection, experimental and simulated distributions were compared for all kinematical variables. A strong background rejection together with a good efficiency could be achieved with cuts at $\pm 3\sigma$.

Two examples of experimental distributions are given in fig. 2 with the invariant mass of the η decaying in two γ-rays and the missing mass calculated from the recoil proton momentum; they are compared with what is expected from the simulation of the ηp channel. For both quantities, with all kinematical cuts applied, an overall satisfactory agreement is achieved, despite some slight discrepancies. These are attributed to small misalignments of the apparatus (beam, target, wire chambers, . . .) not fully taken
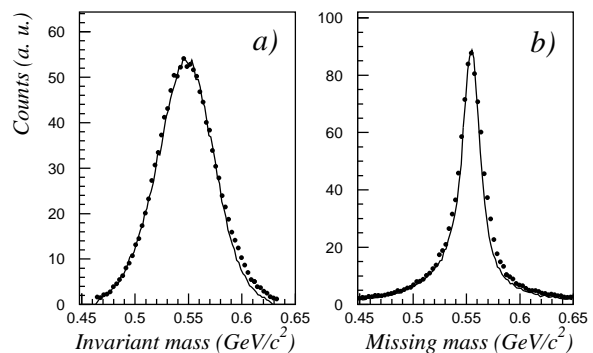

Fig. 2. (a) Invariant-mass spectrum for $\eta \to 2\gamma$. (b) Missing-mass spectrum calculated from the proton momentum. Data (closed circles) and simulation of the ηp channel (solid line) are compared with all kinematical cuts applied.

into account in the simulation. Indeed, similar discrepancies remain when varying cuts from $\pm 3\sigma$ to $\pm 2\sigma$, excluding therefore a significant background contribution.

The level of hadronic background, estimated from the simulation of all possible final states, does not exceed 1% at 1 GeV and increases up to 5% at 1.5 GeV. Such a limited contamination was confirmed by the good agreement of the asymmetries and differential cross-sections extracted independently for the two neutral η decay modes (see sect. 4.2).

3.2 Measurement of Σ

The beam asymmetry Σ was determined from the standard expression:

$$\frac{\tilde{N}_V(\varphi) - \tilde{N}_H(\varphi)}{\tilde{N}_V(\varphi) + \tilde{N}_H(\varphi)} = P_\gamma \Sigma \cos(2\varphi), \tag{1}$$

where $\tilde{N}_V$ and $\tilde{N}_H$ are the azimuthal yields normalized by the integrated flux for the vertical and horizontal polarization states, respectively. P_γ is the degree of linear polarization of the beam and φ the azimuthal angle of the reaction plane. For a given bin in energy E_γ and θ_{cm}, with θ_{cm} the η center-of-mass angle, the beam asymmetry Σ was extracted from the fit of the normalized ratio (eq. (1)) by the function $P_\gamma \Sigma \cos(2\varphi)$, using the known energy dependence of P_γ. The measured asymmetries were corrected for the finite φ binning ($\Sigma_{true} = \Sigma_{meas}(1 + R_\varphi)$ with $R_\varphi = 0.026$ for 16 bins).

Two sources of systematic errors were considered: i) the uncertainty on the beam polarization ($\delta\Sigma/\Sigma = \delta P_\gamma/P_\gamma = 2\%$) and ii) the background contamination. For the second one, two main contributions were identified: other photoproduction (hadronic) reactions and target wall events. The uncertainty due to hadronic contamination was estimated from the variation of the extracted asymmetries when opening cuts from $\pm 3\sigma$ to $\pm 4\sigma$. The resulting errors range from $\delta\Sigma = 0.003$ to 0.035. The rate of target wall events was measured via empty target runs
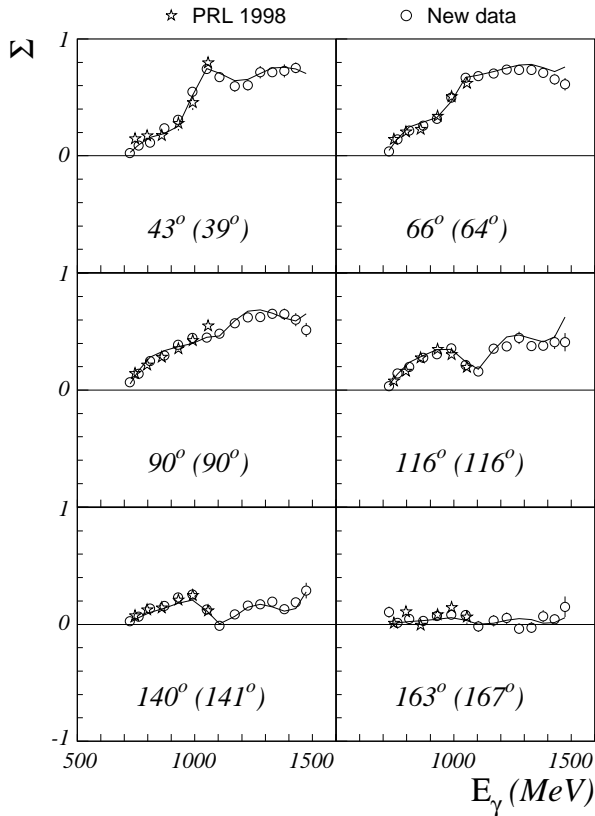
Fig. 3. Beam asymmetry as a function of the γ-ray energy for different η center-of-mass angles. Results published in 1998 up to 1100 MeV (stars —angle in parenthesis) are compared to the new results (circles). The curve represents the result of the BCC model (see sect. 4.5).

Fig. 4. Differential cross-section for photon energies ranging from 850 to 1100 MeV. Results published in 2002 (stars —energy in parenthesis) are compared to the new results (circles).

and found to be less than 1%. The corresponding error was neglected. All systematic and statistical errors were summed quadratically. The global statistical/systematic ratio was found to be of the order of 1.5.

3.3 Measurement of dσ/dΩ

The differential cross-section for a given bin in E_γ and $\cos\theta_{cm}$ was calculated using the following expression:

$$\frac{\mathrm{d}\sigma}{\mathrm{d}\Omega}(\cos\theta_{cm}, E_\gamma) = \frac{N(\cos\theta_{cm}, E_\gamma)}{b_\eta\epsilon(\cos\theta_{cm}, E_\gamma)F(E_\gamma)\rho l\Delta\Omega}, \quad (2)$$

where N is the number of selected events, b_η the branching ratio, ϵ the detection efficiency, F the integrated beam flux, ρ the hydrogen density, l the target length and $\Delta\Omega$ the solid angle (in the present case $\Delta\Omega = 0.2\pi$, corresponding to 20 bins in $\cos\theta_{cm}$).

The detection efficiency ϵ was derived from the simulation. The global efficiency, including acceptance, detection, identification and selection, is of the order of 33% for $\eta \to 2\gamma$ and 6% for $\eta \to 3\pi^0$.

Since cross-section data were obtained by summation of a large number of successive periods, the corresponding experimental configurations were implemented in the
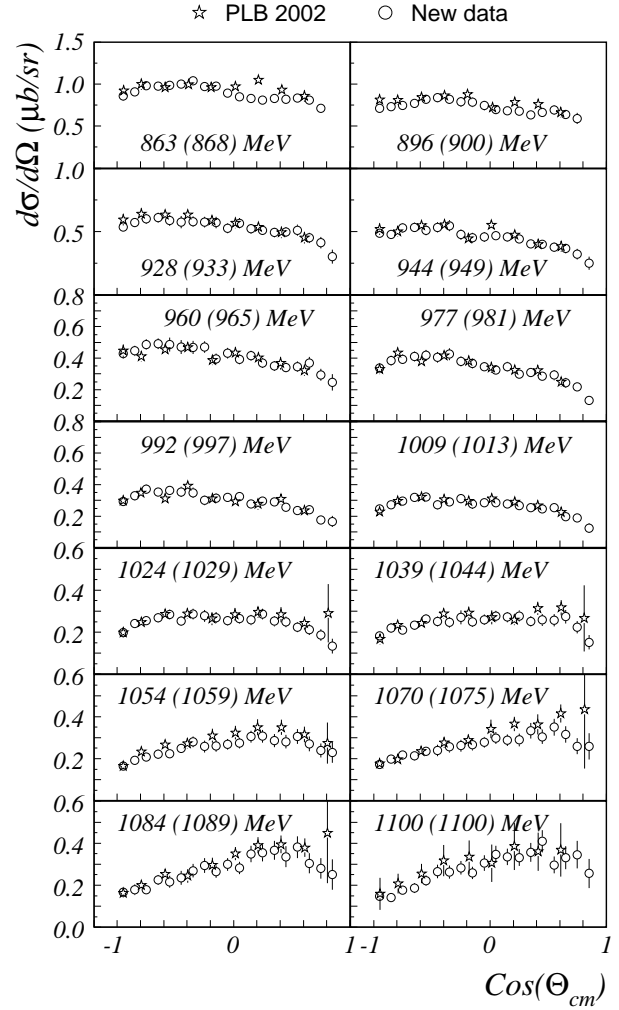
simulation to calculate the efficiency. In particular, special care was taken of the longitudinal position of the target, measured with the cylindrical MWPCs [17], a crucial parameter for the control of the acceptance.

Two types of systematic errors were taken into account: global and bin-dependent ones. The former type includes the uncertainties on beam flux monitor efficiency, hydrogen density and target length. The quadratic sum of these different contributions gives a global normalization error of 2.3%. The latter type takes into account uncertainties on longitudinal target position, efficiency and hadronic background contamination. The errors corresponding to the target position strongly depend on the bin; they are in general low ($\leq 2\%$) and can reach up to 10% for a few points. The error due to hadronic contamination, together with the error on efficiency, were estimated from the variation of the extracted cross-sections when opening cuts from $\pm 3\sigma$ to $\pm 4\sigma$. The resulting uncertainties (angular averaged) steadily increase from

Table 1. Beam asymmetry Σ as a function of the photon laboratory energy and the η center-of-mass angle.

$\theta_{cm}(°)$	$E_\gamma = 724\,\mathrm{MeV}$	$\theta_{cm}(°)$	$E_\gamma = 761\,\mathrm{MeV}$	$\theta_{cm}(°)$	$E_\gamma = 810\,\mathrm{MeV}$	$\theta_{cm}(°)$	$E_\gamma = 870\,\mathrm{MeV}$
33.4	0.036 ± 0.034	35.4	0.093 ± 0.018	36.1	0.100 ± 0.018	38.7	0.182 ± 0.026
52.6	0.061 ± 0.023	53.1	0.103 ± 0.015	53.3	0.159 ± 0.019	53.6	0.246 ± 0.015
66.4	0.031 ± 0.040	66.5	0.167 ± 0.021	66.7	0.226 ± 0.030	66.5	0.243 ± 0.019
78.4	0.016 ± 0.045	78.5	0.132 ± 0.021	78.8	0.235 ± 0.022	78.5	0.305 ± 0.020
90.0	0.092 ± 0.045	90.0	0.143 ± 0.021	90.3	0.259 ± 0.018	90.2	0.295 ± 0.018
101.6	0.049 ± 0.045	101.5	0.136 ± 0.019	101.8	0.243 ± 0.016	101.8	0.288 ± 0.020
113.9	0.031 ± 0.051	113.6	0.150 ± 0.021	113.8	0.200 ± 0.015	114.0	0.293 ± 0.020
127.1	0.052 ± 0.040	127.1	0.117 ± 0.020	126.9	0.170 ± 0.017	127.0	0.233 ± 0.012
144.5	0.019 ± 0.045	143.9	0.054 ± 0.019	143.6	0.128 ± 0.016	143.4	0.138 ± 0.013
159.8	0.060 ± 0.035	160.8	0.022 ± 0.013	161.0	0.050 ± 0.013	161.1	0.047 ± 0.010

$\theta_{cm}(°)$	$E_\gamma = 929\,\mathrm{MeV}$	$\theta_{cm}(°)$	$E_\gamma = 990\,\mathrm{MeV}$	$\theta_{cm}(°)$	$E_\gamma = 1051\,\mathrm{MeV}$	$\theta_{cm}(°)$	$E_\gamma = 1105\,\mathrm{MeV}$
40.1	0.285 ± 0.028	40.1	0.497 ± 0.036	39.9	0.750 ± 0.032	40.1	0.742 ± 0.045
53.5	0.310 ± 0.021	53.7	0.486 ± 0.022	53.8	0.713 ± 0.022	53.8	0.702 ± 0.026
66.6	0.299 ± 0.030	66.6	0.494 ± 0.033	66.5	0.686 ± 0.033	66.5	0.687 ± 0.032
78.5	0.372 ± 0.022	78.6	0.484 ± 0.028	78.6	0.553 ± 0.025	78.5	0.623 ± 0.032
89.9	0.402 ± 0.021	90.0	0.437 ± 0.022	89.9	0.450 ± 0.028	90.0	0.467 ± 0.031
101.9	0.355 ± 0.024	101.7	0.424 ± 0.025	101.5	0.306 ± 0.026	101.3	0.338 ± 0.028
113.9	0.287 ± 0.019	113.8	0.371 ± 0.023	113.9	0.242 ± 0.026	113.8	0.168 ± 0.028
127.3	0.310 ± 0.017	127.4	0.307 ± 0.018	127.4	0.162 ± 0.023	127.5	0.053 ± 0.023
143.4	0.203 ± 0.015	143.5	0.244 ± 0.018	143.4	0.120 ± 0.018	143.2	-0.019 ± 0.022
160.9	0.077 ± 0.014	160.7	0.104 ± 0.019	160.6	0.080 ± 0.019	160.5	-0.026 ± 0.033

$\theta_{cm}(°)$	$E_\gamma = 1170\,\mathrm{MeV}$	$\theta_{cm}(°)$	$E_\gamma = 1225\,\mathrm{MeV}$	$\theta_{cm}(°)$	$E_\gamma = 1278\,\mathrm{MeV}$	$\theta_{cm}(°)$	$E_\gamma = 1330\,\mathrm{MeV}$
39.6	0.568 ± 0.051	39.7	0.536 ± 0.048	39.9	0.748 ± 0.077	40.0	0.694 ± 0.051
53.8	0.667 ± 0.031	53.8	0.701 ± 0.036	53.9	0.671 ± 0.029	53.7	0.763 ± 0.042
66.5	0.690 ± 0.041	66.6	0.748 ± 0.045	66.5	0.745 ± 0.031	66.6	0.744 ± 0.039
78.5	0.668 ± 0.040	78.5	0.716 ± 0.051	78.5	0.684 ± 0.040	78.6	0.697 ± 0.045
89.9	0.601 ± 0.041	90.0	0.608 ± 0.041	89.9	0.634 ± 0.046	90.1	0.645 ± 0.055
101.3	0.493 ± 0.051	101.2	0.549 ± 0.038	101.2	0.594 ± 0.043	101.3	0.567 ± 0.041
113.8	0.382 ± 0.061	113.8	0.437 ± 0.054	113.9	0.482 ± 0.064	113.8	0.422 ± 0.057
127.4	0.138 ± 0.040	127.5	0.243 ± 0.032	127.6	0.252 ± 0.033	127.7	0.264 ± 0.050
143.1	0.085 ± 0.036	143.2	0.132 ± 0.028	143.2	0.176 ± 0.028	143.3	0.172 ± 0.028
160.2	0.009 ± 0.030	160.4	0.048 ± 0.035	160.4	-0.009 ± 0.028	160.3	0.006 ± 0.033

$\theta_{cm}(°)$	$E_\gamma = 1381\,\mathrm{MeV}$	$\theta_{cm}(°)$	$E_\gamma = 1424\,\mathrm{MeV}$	$\theta_{cm}(°)$	$E_\gamma = 1472\,\mathrm{MeV}$
40.2	0.720 ± 0.072	40.8	0.646 ± 0.073	40.2	0.727 ± 0.147
53.5	0.760 ± 0.045	54.1	0.750 ± 0.041	53.8	0.771 ± 0.080
66.5	0.710 ± 0.059	64.6	0.716 ± 0.048	64.6	0.601 ± 0.051
78.5	0.712 ± 0.056	77.5	0.661 ± 0.060	77.4	0.581 ± 0.052
89.9	0.663 ± 0.053	90.0	0.623 ± 0.054	90.0	0.563 ± 0.062
101.1	0.551 ± 0.042	100.6	0.556 ± 0.055	100.6	0.483 ± 0.076
113.7	0.401 ± 0.053	113.0	0.419 ± 0.076	113.0	0.484 ± 0.091
127.6	0.252 ± 0.032	127.5	0.314 ± 0.028	127.6	0.380 ± 0.064
143.3	0.101 ± 0.028	142.5	0.160 ± 0.023	142.2	0.282 ± 0.059
160.2	0.056 ± 0.038	160.3	0.038 ± 0.027	160.8	0.074 ± 0.063

around 4% at 1 GeV up to 13% at 1.5 GeV. Only the bin-dependent errors were summed quadratically with the statistical errors. The global statistical/systematic ratio was found to be of the order of 1.1.

4 Results and discussions

The complete set of asymmetry and cross-section data ($\sim$ 1 million selected ηp events) covers large photon energy (from 700 to 1500 MeV) and η angular ($\theta_{cm} = 30$–$160°$) ranges. The results are displayed in figs. 3 to 14. Numerical values are listed in tables 1 to 4. For cross-sections, the global normalization uncertainty of 2.3% has not been

included in the tabulated values nor in the plotted errors. The total cross-section was also extracted and is plotted in fig. 8. Up to 850 MeV, the presented cross-sections are those previously published which were obtained with a 3 cm long target better suited for the detection of low-energy protons.

4.1 Comparison to previous GRAAL results

GRAAL results were already published for γ-ray energies up to 1100 MeV (Σ [2] and $d\sigma/d\Omega$ [4]). The newly analyzed sample not only extends the energy range up to 1500 MeV but also increases tenfold the statistics.

Table 2. Differential cross-section $d\sigma/d\Omega$ (μb/sr) as a function of the photon laboratory energy (700–850 MeV) and the cosine of the η center-of-mass angle.

$\cos(\theta_{cm})$	$E_\gamma = 714$ MeV	$\cos(\theta_{cm})$	$E_\gamma = 732$ MeV	$\cos(\theta_{cm})$	$E_\gamma = 749$ MeV	$\cos(\theta_{cm})$	$E_\gamma = 766$ MeV
-0.85	0.588 ± 0.077	-0.91	1.007 ± 0.064	-0.92	1.108 ± 0.060	-0.93	1.253 ± 0.065
-0.62	0.499 ± 0.048	-0.74	0.903 ± 0.060	-0.76	1.102 ± 0.069	-0.77	1.158 ± 0.077
-0.46	0.517 ± 0.057	-0.54	0.884 ± 0.074	-0.56	1.180 ± 0.089	-0.57	1.244 ± 0.085
-0.30	0.534 ± 0.059	-0.35	0.921 ± 0.090	-0.38	1.246 ± 0.083	-0.38	1.230 ± 0.068
-0.21	0.523 ± 0.067	-0.20	0.927 ± 0.094	-0.20	1.181 ± 0.070	-0.19	1.246 ± 0.053
-0.03	0.499 ± 0.067	-0.02	0.839 ± 0.073	0.00	1.169 ± 0.068	0.01	1.301 ± 0.053
0.12	0.512 ± 0.060	0.17	0.863 ± 0.082	0.19	1.135 ± 0.063	0.21	1.143 ± 0.055
0.29	0.575 ± 0.065	0.38	0.985 ± 0.085	0.38	1.231 ± 0.074	0.40	1.342 ± 0.062
0.49	0.577 ± 0.050	0.59	0.928 ± 0.292	0.58	1.242 ± 0.214	0.58	1.170 ± 0.069
0.81	0.596 ± 0.088	0.81	0.943 ± 0.784	0.79	0.876 ± 0.637	0.78	1.077 ± 0.281
$\cos(\theta_{cm})$	$E_\gamma = 785$ MeV	$\cos(\theta_{cm})$	$E_\gamma = 801$ MeV	$\cos(\theta_{cm})$	$E_\gamma = 818$ MeV	$\cos(\theta_{cm})$	$E_\gamma = 835$ MeV
-0.94	1.220 ± 0.073	-0.94	1.228 ± 0.067	-0.94	1.170 ± 0.067	-0.94	1.007 ± 0.066
-0.78	1.289 ± 0.086	-0.79	1.213 ± 0.081	-0.79	1.144 ± 0.076	-0.79	1.082 ± 0.072
-0.58	1.240 ± 0.079	-0.58	1.245 ± 0.065	-0.59	1.214 ± 0.058	-0.59	1.117 ± 0.052
-0.39	1.286 ± 0.060	-0.38	1.230 ± 0.050	-0.38	1.165 ± 0.047	-0.38	1.167 ± 0.048
-0.19	1.281 ± 0.056	-0.19	1.257 ± 0.054	-0.19	1.268 ± 0.059	-0.19	1.172 ± 0.053
0.01	1.255 ± 0.056	0.01	1.251 ± 0.057	0.00	1.320 ± 0.062	0.01	1.121 ± 0.059
0.21	1.305 ± 0.067	0.20	1.324 ± 0.064	0.21	1.194 ± 0.062	0.22	1.117 ± 0.060
0.41	1.300 ± 0.066	0.40	1.160 ± 0.071	0.41	1.231 ± 0.067	0.41	1.109 ± 0.059
0.60	1.212 ± 0.071	0.60	1.186 ± 0.079	0.60	1.341 ± 0.092	0.61	1.097 ± 0.082
0.79	1.287 ± 0.130	0.79	1.181 ± 0.097	0.79	1.075 ± 0.134	0.80	1.046 ± 0.393

The new results are compared with the published data in figs. 3 (Σ) and 4 ($d\sigma/d\Omega$ for $E_\gamma \geq 850$ MeV). The agreement between the two sets is good at all energies and angles. For the beam asymmetries, it should be remembered that the beam polarization depends upon the energy and the used laser line. Hence, at a given energy, the beam polarization differs for the UV and green laser lines; for instance, at 1 GeV, $P_\gamma \simeq 100\%$ for green and $\simeq 70\%$ for UV. The excellent agreement confirms the good control of the beam polarization. For the cross-sections, the comparison is even more stringent. Indeed, these absolute measurements necessitate an accurate knowledge of the flux and efficiency; on top of that, the summation over numerous periods requires a precise monitoring of the detector response. Again, the observed good agreement between the two data sets demonstrates the reliability of the present analysis.

These new results improve our previous measurements particularly at forward angles and allow to better describe the behaviour of the cross-section in this angular domain.

4.2 Comparison between the two η neutral decays

The beam asymmetries and differential cross-sections were calculated independently for the two neutral decay modes, $\eta \to 2\gamma$ and $\eta \to 3\pi^0$ and the comparison is displayed in figs. 5 (Σ) and 6 ($d\sigma/d\Omega$). To reduce statistical errors associated with the $3\pi^0$ decay, a broader angular binning was used for the comparison.

Because the detection of the six decay photons is requested in the $3\pi^0$ analysis, the global efficiency is strongly reduced as compared to the 2γ (see sect. 3.3) (the angular range is also limited to $\theta_{cm} \geq 60°$). On the other hand,

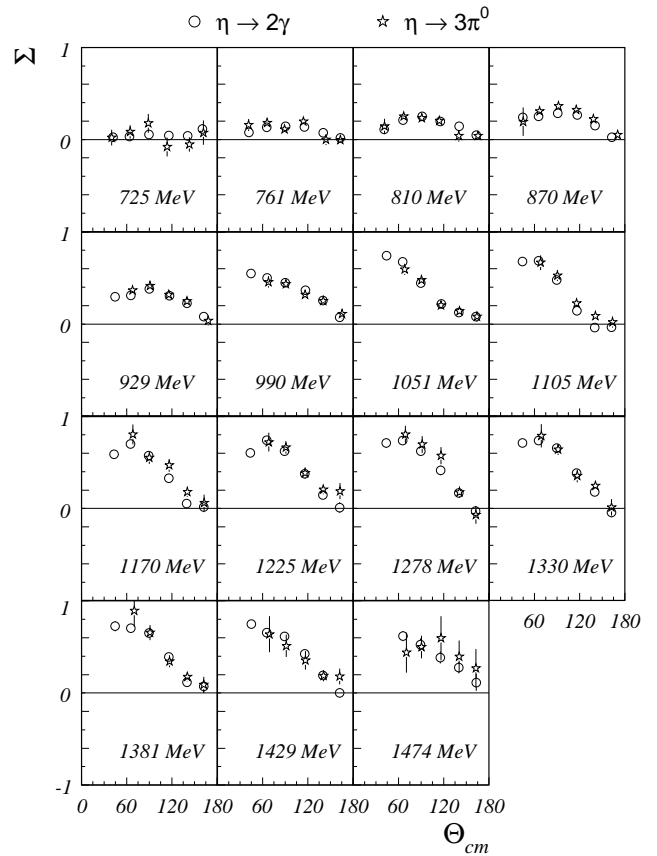
Fig. 5. Angular distributions of the beam asymmetry. Comparison between the two neutral decay modes: $\eta \to 2\gamma$ (circles) and $\eta \to 3\pi^0$ (stars).

Table 3. Differential cross-section $d\sigma/d\Omega$ (μb/sr) as a function of the photon laboratory energy (850–1200 MeV) and the cosine of the η center-of-mass angle.

$\cos(\theta_{cm})$	$E_\gamma = 863\,\text{MeV}$	$\cos(\theta_{cm})$	$E_\gamma = 896\,\text{MeV}$	$\cos(\theta_{cm})$	$E_\gamma = 928\,\text{MeV}$	$\cos(\theta_{cm})$	$E_\gamma = 962\,\text{MeV}$
−0.95	0.858 ± 0.052	−0.95	0.707 ± 0.042	−0.95	0.542 ± 0.030	−0.95	0.414 ± 0.024
−0.85	0.906 ± 0.045	−0.85	0.738 ± 0.044	−0.85	0.582 ± 0.033	−0.85	0.424 ± 0.025
−0.75	0.980 ± 0.044	−0.75	0.778 ± 0.041	−0.75	0.604 ± 0.031	−0.75	0.475 ± 0.025
−0.65	0.976 ± 0.038	−0.65	0.771 ± 0.032	−0.65	0.615 ± 0.032	−0.65	0.476 ± 0.027
−0.55	0.984 ± 0.038	−0.55	0.808 ± 0.035	−0.55	0.589 ± 0.034	−0.55	0.467 ± 0.032
−0.45	1.001 ± 0.038	−0.45	0.831 ± 0.038	−0.45	0.599 ± 0.039	−0.45	0.455 ± 0.035
−0.35	1.042 ± 0.044	−0.35	0.825 ± 0.042	−0.35	0.616 ± 0.031	−0.35	0.465 ± 0.032
−0.25	0.971 ± 0.040	−0.25	0.805 ± 0.044	−0.25	0.584 ± 0.034	−0.25	0.434 ± 0.026
−0.15	0.978 ± 0.043	−0.15	0.769 ± 0.040	−0.15	0.568 ± 0.036	−0.15	0.392 ± 0.026
−0.05	0.895 ± 0.047	−0.05	0.749 ± 0.042	−0.05	0.546 ± 0.032	−0.05	0.406 ± 0.023
0.05	0.849 ± 0.043	0.05	0.686 ± 0.036	0.05	0.548 ± 0.027	0.05	0.384 ± 0.020
0.15	0.831 ± 0.047	0.15	0.685 ± 0.033	0.15	0.516 ± 0.027	0.15	0.399 ± 0.022
0.25	0.809 ± 0.036	0.25	0.683 ± 0.033	0.25	0.514 ± 0.027	0.25	0.366 ± 0.021
0.35	0.827 ± 0.038	0.35	0.661 ± 0.032	0.35	0.479 ± 0.026	0.35	0.346 ± 0.023
0.45	0.818 ± 0.038	0.45	0.640 ± 0.033	0.45	0.480 ± 0.028	0.45	0.340 ± 0.022
0.55	0.832 ± 0.041	0.55	0.686 ± 0.040	0.55	0.490 ± 0.030	0.55	0.334 ± 0.025
0.65	0.809 ± 0.043	0.65	0.632 ± 0.039	0.65	0.458 ± 0.030	0.65	0.329 ± 0.028
0.75	0.711 ± 0.045	0.75	0.609 ± 0.046	0.75	0.407 ± 0.032	0.75	0.282 ± 0.027
				0.85	0.300 ± 0.040	0.85	0.210 ± 0.033

$\cos(\theta_{cm})$	$E_\gamma = 992\,\text{MeV}$	$\cos(\theta_{cm})$	$E_\gamma = 1024\,\text{MeV}$	$\cos(\theta_{cm})$	$E_\gamma = 1055\,\text{MeV}$	$\cos(\theta_{cm})$	$E_\gamma = 1084\,\text{MeV}$
−0.95	0.296 ± 0.022	−0.95	0.206 ± 0.016	−0.95	0.168 ± 0.016	−0.95	0.164 ± 0.020
−0.85	0.334 ± 0.025	−0.85	0.239 ± 0.019	−0.85	0.199 ± 0.018	−0.85	0.171 ± 0.019
−0.75	0.358 ± 0.022	−0.75	0.248 ± 0.018	−0.75	0.214 ± 0.017	−0.75	0.190 ± 0.018
−0.65	0.360 ± 0.023	−0.65	0.270 ± 0.018	−0.65	0.221 ± 0.019	−0.65	0.218 ± 0.019
−0.55	0.368 ± 0.021	−0.55	0.295 ± 0.018	−0.55	0.230 ± 0.017	−0.55	0.232 ± 0.020
−0.45	0.348 ± 0.025	−0.45	0.262 ± 0.019	−0.45	0.241 ± 0.017	−0.45	0.252 ± 0.029
−0.35	0.353 ± 0.025	−0.35	0.275 ± 0.018	−0.35	0.264 ± 0.021	−0.35	0.257 ± 0.022
−0.25	0.330 ± 0.024	−0.25	0.279 ± 0.023	−0.25	0.269 ± 0.023	−0.25	0.272 ± 0.024
−0.15	0.325 ± 0.023	−0.15	0.268 ± 0.021	−0.15	0.249 ± 0.021	−0.15	0.269 ± 0.024
−0.05	0.317 ± 0.019	−0.05	0.262 ± 0.018	−0.05	0.268 ± 0.020	−0.05	0.282 ± 0.021
0.05	0.319 ± 0.019	0.05	0.272 ± 0.018	0.05	0.276 ± 0.019	0.05	0.305 ± 0.024
0.15	0.293 ± 0.018	0.15	0.266 ± 0.018	0.15	0.288 ± 0.020	0.15	0.349 ± 0.027
0.25	0.288 ± 0.019	0.25	0.280 ± 0.017	0.25	0.292 ± 0.021	0.25	0.315 ± 0.025
0.35	0.288 ± 0.018	0.35	0.248 ± 0.017	0.35	0.287 ± 0.023	0.35	0.382 ± 0.035
0.45	0.256 ± 0.018	0.45	0.253 ± 0.022	0.45	0.280 ± 0.023	0.45	0.343 ± 0.036
0.55	0.258 ± 0.023	0.55	0.235 ± 0.018	0.55	0.302 ± 0.027	0.55	0.351 ± 0.035
0.65	0.231 ± 0.022	0.65	0.212 ± 0.019	0.65	0.297 ± 0.027	0.65	0.299 ± 0.036
0.75	0.189 ± 0.019	0.75	0.193 ± 0.021	0.75	0.240 ± 0.024	0.75	0.282 ± 0.042
0.85	0.146 ± 0.022	0.85	0.134 ± 0.026	0.85	0.208 ± 0.033	0.85	0.262 ± 0.056

| $\cos(\theta_{cm})$	$E_\gamma = 1115\,\text{MeV}$	$\cos(\theta_{cm})$	$E_\gamma = 1145\,\text{MeV}$	$\cos(\theta_{cm})$	$E_\gamma = 1174\,\text{MeV}$	$\cos(\theta_{cm})$	$E_\gamma = 1203\,\text{MeV}$
−0.95	0.122 ± 0.014	−0.95	0.105 ± 0.014	−0.95	0.103 ± 0.014	−0.95	0.090 ± 0.009
−0.85	0.153 ± 0.020	−0.85	0.119 ± 0.018	−0.85	0.110 ± 0.016	−0.85	0.116 ± 0.016
−0.75	0.175 ± 0.018	−0.75	0.136 ± 0.017	−0.75	0.133 ± 0.017	−0.75	0.122 ± 0.016
−0.65	0.170 ± 0.017	−0.65	0.166 ± 0.017	−0.65	0.157 ± 0.014	−0.65	0.138 ± 0.016
−0.55	0.199 ± 0.022	−0.55	0.175 ± 0.017	−0.55	0.172 ± 0.018	−0.55	0.167 ± 0.018
−0.45	0.232 ± 0.029	−0.45	0.219 ± 0.022	−0.45	0.184 ± 0.021	−0.45	0.181 ± 0.017
−0.35	0.250 ± 0.024	−0.35	0.231 ± 0.024	−0.35	0.220 ± 0.023	−0.35	0.228 ± 0.025
−0.25	0.283 ± 0.026	−0.25	0.249 ± 0.023	−0.25	0.254 ± 0.023	−0.25	0.249 ± 0.031
−0.15	0.272 ± 0.024	−0.15	0.241 ± 0.022	−0.15	0.274 ± 0.025	−0.15	0.234 ± 0.022
−0.05	0.298 ± 0.025	−0.05	0.258 ± 0.020	−0.05	0.275 ± 0.026	−0.05	0.264 ± 0.026
0.05	0.298 ± 0.024	0.05	0.333 ± 0.028	0.05	0.297 ± 0.027	0.05	0.265 ± 0.023
0.15	0.317 ± 0.030	0.15	0.284 ± 0.024	0.15	0.286 ± 0.027	0.15	0.260 ± 0.026
0.25	0.364 ± 0.032	0.25	0.297 ± 0.032	0.25	0.320 ± 0.036	0.25	0.318 ± 0.038
0.35	0.325 ± 0.035	0.35	0.342 ± 0.038	0.35	0.301 ± 0.032	0.35	0.296 ± 0.039
0.45	0.332 ± 0.032	0.45	0.355 ± 0.038	0.45	0.310 ± 0.032	0.45	0.345 ± 0.041
0.55	0.345 ± 0.039	0.55	0.318 ± 0.037	0.55	0.357 ± 0.044	0.55	0.340 ± 0.043
0.65	0.343 ± 0.041	0.65	0.356 ± 0.046	0.65	0.322 ± 0.038	0.65	0.326 ± 0.053
0.75	0.361 ± 0.051	0.75	0.304 ± 0.049	0.75	0.312 ± 0.054	0.75	0.335 ± 0.055
0.85	0.325 ± 0.060	0.85	0.253 ± 0.054	0.85	0.322 ± 0.065	0.85	0.295 ± 0.075
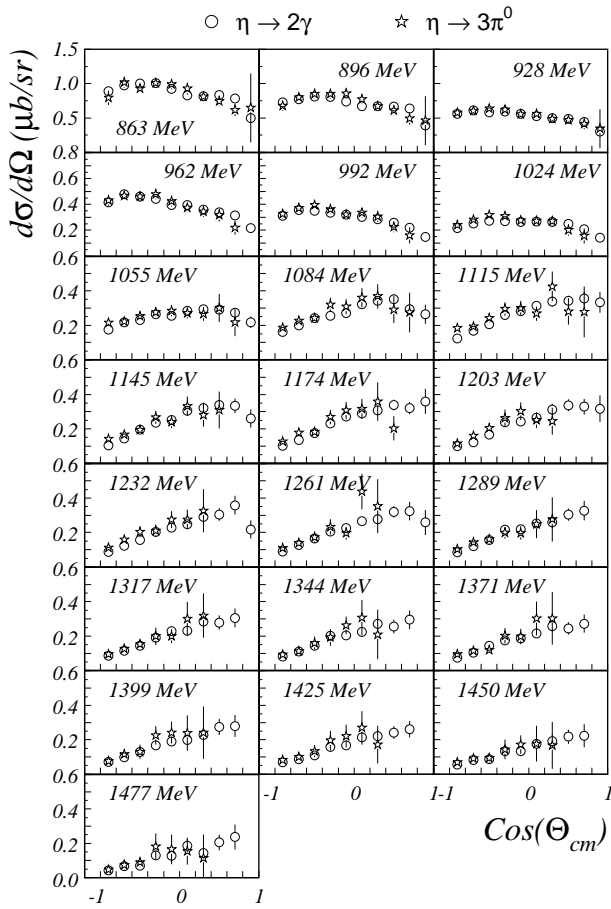
Fig. 6. Differential cross-section for energies ranging from 850 to 1500 MeV. Comparison between the two neutral decay modes: $\eta \to 2\gamma$ (circles) and $\eta \to 3\pi^0$ (stars).

this criterion largely excludes the two main hadronic backgrounds (π^0 and $2\pi^0$). The excellent agreement observed for both quantities between the 2γ and $3\pi^0$ results confirms the low level of background in the 2γ channel. In addition, the very good agreement of the cross-section data demonstrates the reliability of the Monte Carlo simulation, especially for the cluster reconstruction in the BGO calorimeter.

4.3 Comparison to CLAS, CB-ELSA and LNS-GeV-γ results

Differential cross-section results have been recently published by the CLAS [6], CB-ELSA [7] and LNS-GeV-γ [8] Collaborations. Whereas the GRAAL data (as well as LNS-GeV-γ results) are absolute measurements, for the CLAS and CB-ELSA results, the normalization was obtained by using the SAID partial-wave analysis.

The comparison between GRAAL, CLAS, CB-ELSA and LNS-GeV-γ data is shown in fig. 11 for the closest energy bins. The overall agreement is good over the who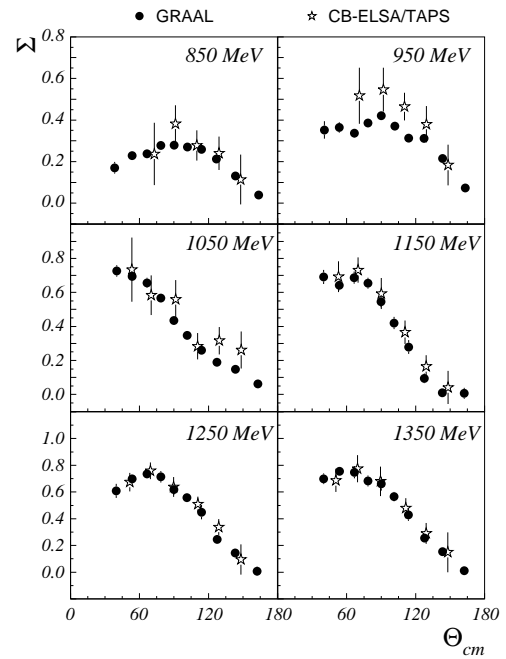le energy and angular ranges. It is worth noting that our angular range is complementary to the CLAS and CB-ELSA ones, extending the measurement to more backward angles.

Fig. 7. Comparison between GRAAL (closed circles) and CB-ELSA/TAPS (open stars) beam asymmetry data for the Bonn energy bins (± 50 MeV).
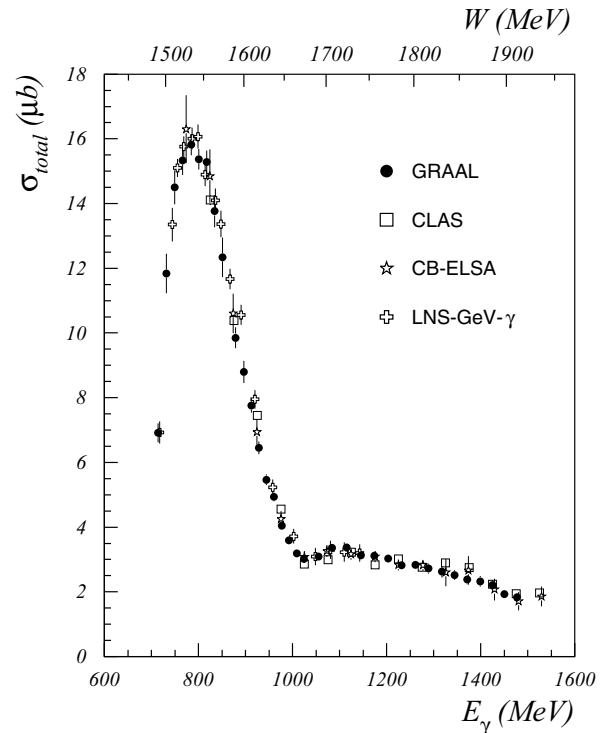

Fig. 8. Estimated total cross-section. The GRAAL results (closed circles) are compared with CLAS (open squares), CB-ELSA (open stars) and LNS-GeV-γ (open crosses) data.

Table 4. Differential cross-section $\mathrm{d}\sigma/\mathrm{d}\Omega$ (μb/sr) as a function of the photon laboratory energy (1200–1500 MeV) and the cosine of the η center-of-mass angle.

$\cos(\theta_{cm})$	$E_\gamma = 1232\,\mathrm{MeV}$	$\cos(\theta_{cm})$	$E_\gamma = 1261\,\mathrm{MeV}$	$\cos(\theta_{cm})$	$E_\gamma = 1289\,\mathrm{MeV}$	$\cos(\theta_{cm})$	$E_\gamma = 1317\,\mathrm{MeV}$
-0.95	0.080 ± 0.010	-0.95	0.086 ± 0.012	-0.95	0.078 ± 0.012	-0.95	0.076 ± 0.013
-0.85	0.105 ± 0.013	-0.85	0.103 ± 0.018	-0.85	0.102 ± 0.012	-0.85	0.100 ± 0.016
-0.75	0.121 ± 0.014	-0.75	0.120 ± 0.016	-0.75	0.123 ± 0.015	-0.75	0.106 ± 0.014
-0.65	0.139 ± 0.012	-0.65	0.143 ± 0.014	-0.65	0.127 ± 0.013	-0.65	0.131 ± 0.014
-0.55	0.164 ± 0.020	-0.55	0.155 ± 0.015	-0.55	0.142 ± 0.016	-0.55	0.129 ± 0.017
-0.45	0.168 ± 0.019	-0.45	0.181 ± 0.021	-0.45	0.178 ± 0.024	-0.45	0.169 ± 0.023
-0.35	0.206 ± 0.022	-0.35	0.204 ± 0.025	-0.35	0.208 ± 0.023	-0.35	0.186 ± 0.028
-0.25	0.200 ± 0.021	-0.25	0.212 ± 0.024	-0.25	0.217 ± 0.024	-0.25	0.193 ± 0.021
-0.15	0.229 ± 0.022	-0.15	0.229 ± 0.023	-0.15	0.226 ± 0.027	-0.15	0.213 ± 0.022
-0.05	0.236 ± 0.024	-0.05	0.216 ± 0.022	-0.05	0.206 ± 0.024	-0.05	0.235 ± 0.026
0.05	0.239 ± 0.023	0.05	0.258 ± 0.027	0.05	0.235 ± 0.024	0.05	0.231 ± 0.028
0.15	0.264 ± 0.026	0.15	0.305 ± 0.035	0.15	0.272 ± 0.032	0.15	0.240 ± 0.036
0.25	0.282 ± 0.033	0.25	0.294 ± 0.043	0.25	0.251 ± 0.040	0.25	0.269 ± 0.049
0.35	0.306 ± 0.037	0.35	0.267 ± 0.038	0.35	0.270 ± 0.039	0.35	0.307 ± 0.038
0.45	0.285 ± 0.043	0.45	0.312 ± 0.041	0.45	0.322 ± 0.047	0.45	0.261 ± 0.045
0.55	0.330 ± 0.042	0.55	0.333 ± 0.044	0.55	0.278 ± 0.039	0.55	0.302 ± 0.052
0.65	0.344 ± 0.050	0.65	0.336 ± 0.062	0.65	0.335 ± 0.062	0.65	0.302 ± 0.057
0.75	0.360 ± 0.089	0.75	0.303 ± 0.060	0.75	0.308 ± 0.069	0.75	0.299 ± 0.068
0.85	0.198 ± 0.051	0.85	0.245 ± 0.071				

$\cos(\theta_{cm})$	$E_\gamma = 1344\,\mathrm{MeV}$	$\cos(\theta_{cm})$	$E_\gamma = 1371\,\mathrm{MeV}$	$\cos(\theta_{cm})$	$E_\gamma = 1399\,\mathrm{MeV}$	$\cos(\theta_{cm})$	$E_\gamma = 1425\,\mathrm{MeV}$
-0.95	0.076 ± 0.013	-0.95	0.068 ± 0.012	-0.95	0.068 ± 0.012	-0.95	0.065 ± 0.013
-0.85	0.090 ± 0.012	-0.85	0.093 ± 0.015	-0.85	0.076 ± 0.015	-0.85	0.080 ± 0.014
-0.75	0.108 ± 0.017	-0.75	0.100 ± 0.015	-0.75	0.103 ± 0.014	-0.75	0.087 ± 0.015
-0.65	0.112 ± 0.014	-0.65	0.112 ± 0.012	-0.65	0.099 ± 0.012	-0.65	0.094 ± 0.014
-0.55	0.139 ± 0.017	-0.55	0.120 ± 0.011	-0.55	0.113 ± 0.013	-0.55	0.104 ± 0.015
-0.45	0.162 ± 0.028	-0.45	0.173 ± 0.026	-0.45	0.155 ± 0.023	-0.45	0.132 ± 0.021
-0.35	0.211 ± 0.030	-0.35	0.175 ± 0.027	-0.35	0.166 ± 0.028	-0.35	0.164 ± 0.030
-0.25	0.191 ± 0.025	-0.25	0.177 ± 0.023	-0.25	0.181 ± 0.027	-0.25	0.158 ± 0.022
-0.15	0.197 ± 0.025	-0.15	0.188 ± 0.023	-0.15	0.190 ± 0.021	-0.15	0.160 ± 0.024
-0.05	0.222 ± 0.022	-0.05	0.188 ± 0.025	-0.05	0.200 ± 0.027	-0.05	0.185 ± 0.024
0.05	0.221 ± 0.029	0.05	0.239 ± 0.031	0.05	0.185 ± 0.024	0.05	0.206 ± 0.032
0.15	0.239 ± 0.038	0.15	0.207 ± 0.031	0.15	0.220 ± 0.034	0.15	0.232 ± 0.040
0.25	0.270 ± 0.048	0.25	0.258 ± 0.041	0.25	0.239 ± 0.044	0.25	0.193 ± 0.040
0.35	0.265 ± 0.043	0.35	0.263 ± 0.041	0.35	0.217 ± 0.042	0.35	0.247 ± 0.047
0.45	0.250 ± 0.042	0.45	0.252 ± 0.039	0.45	0.293 ± 0.064	0.45	0.222 ± 0.039
0.55	0.264 ± 0.051	0.55	0.233 ± 0.047	0.55	0.253 ± 0.049	0.55	0.266 ± 0.053
0.65	0.286 ± 0.059	0.65	0.268 ± 0.061	0.65	0.281 ± 0.064	0.65	0.245 ± 0.051
0.75	0.298 ± 0.064	0.75	0.269 ± 0.060	0.75	0.263 ± 0.080	0.75	0.267 ± 0.070

| $\cos(\theta_{cm})$	$E_\gamma = 1450\,\mathrm{MeV}$	$\cos(\theta_{cm})$	$E_\gamma = 1477\,\mathrm{MeV}$
-0.95	0.050 ± 0.013	-0.95	0.034 ± 0.016
-0.85	0.068 ± 0.016	-0.85	0.053 ± 0.016
-0.75	0.077 ± 0.013	-0.75	0.054 ± 0.015
-0.65	0.092 ± 0.010	-0.65	0.087 ± 0.018
-0.55	0.081 ± 0.016	-0.55	0.058 ± 0.012
-0.45	0.099 ± 0.017	-0.45	0.093 ± 0.027
-0.35	0.136 ± 0.026	-0.35	0.130 ± 0.031
-0.25	0.134 ± 0.032	-0.25	0.148 ± 0.032
-0.15	0.139 ± 0.021	-0.15	0.110 ± 0.022
-0.05	0.134 ± 0.025	-0.05	0.156 ± 0.036
0.05	0.179 ± 0.031	0.05	0.201 ± 0.038
0.15	0.174 ± 0.038	0.15	0.164 ± 0.051
0.25	0.170 ± 0.041	0.25	0.142 ± 0.041
0.35	0.225 ± 0.052	0.35	0.144 ± 0.038
0.45	0.227 ± 0.052	0.45	0.251 ± 0.064
0.55	0.208 ± 0.048	0.55	0.164 ± 0.054
0.65	0.214 ± 0.062	0.65	0.177 ± 0.064
0.75	0.213 ± 0.093		
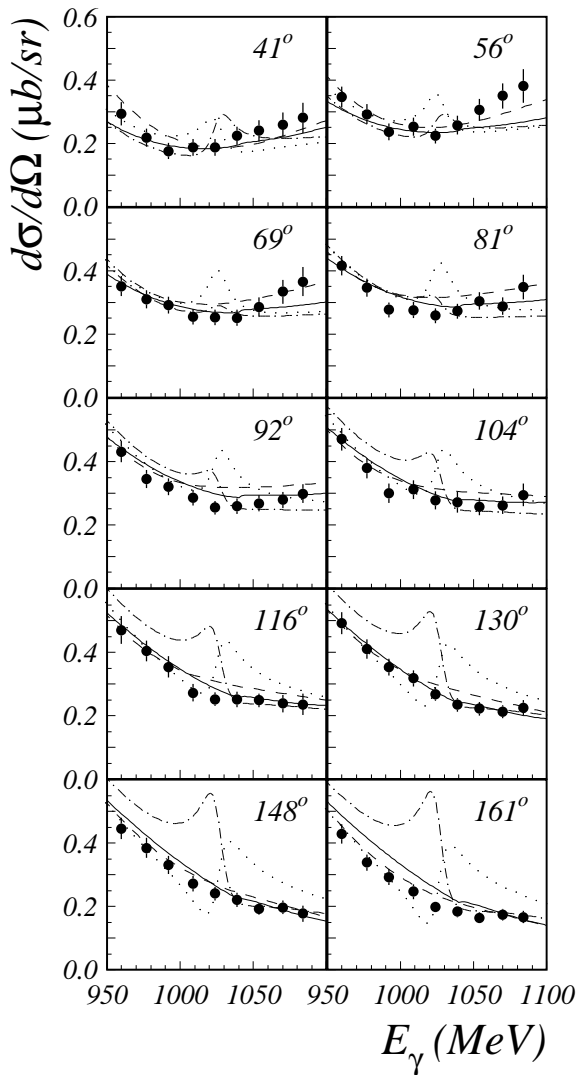
Fig. 9. Differential cross-section between 950 and 1100 MeV obtained with a narrow energy binning for various η center-of-mass angles. Comparison with the standard MAID model (dashed line), BCC partial-wave analysis (solid line) and predictions of the modified reggeized MAID model including a narrow P_{11} state. For this latter model, two versions are displayed corresponding to the two choices for the $\zeta_{\eta N}$ hadronic relative phase (dot-dashed line: $\zeta_{\eta N} = +1$, dotted line: $\zeta_{\eta N} = -1$).

Preliminary beam asymmetries have also been recently presented by the CB-ELSA/TAPS Collaboration in the energy range $E_\gamma = 800$–1400 MeV [9]. The measurements were performed using a linearly polarized tagged photon beam produced by coherent bremsstrahlung off a diamond. A nice agreement is found with our data, except at 950 MeV where sizeable discrepancies are observed (fig. 7).

4.4 Total cross-section

The total cross-section, plotted in fig. 8, was obtained by integration of the measured differential cross-section, using the Bonn-Gatchina model (see sect. 4.5) to extrapolate
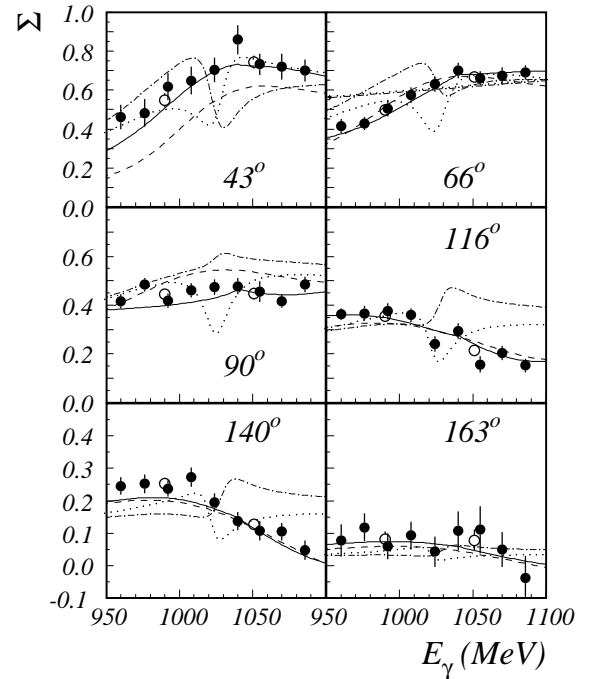
Fig. 10. Beam asymmetry between 950 and 1100 MeV obtained with a narrow energy binning (~ 16 MeV) for various η center-of-mass angles (closed circles). Data corresponding to the large energy binning (~ 60 MeV) presented in fig. 3 are also plotted (open circles). Curve definition as in fig. 9.

to the uncovered forward region (5 to 15% of the full angular range, depending on the energy). The extrapolated fraction amounts between 2 and 15% of the estimated total cross-section for most of the energies. The plotted errors were calculated from the experimental ones and include an additional uncertainty due to the extrapolation procedure. The latter was estimated from the variation of the total cross-section when considering for extrapolation the two other models discussed below, whose behaviours in the most forward region differ from the Bonn-Gatchina model (see figs. 13 and 14). The resulting error represents at the most 5% of the total cross-section.

It should be noted that, despite a good agreement between the differential cross-sections, the new total cross-section is significantly lower than our previous estimate in the 1050–1100 MeV range. This discrepancy mostly originates from the forward region. First, as already stated, the new data are much more precise in this region and clearly indicate a drop of the cross-section at forward angles, not seen before. The integral over the measured range is now lower. Second, in agreement with our data, the model presently used to extrapolate drops at forward angles; it gives therefore a smaller contribution as compared to the simple polynomial fit (degree two) used in our previous publication. Both effects do explain the discrepancy.

Figure 8 displays the comparison with the CLAS [6], CB-ELSA [7] and LNS-GeV-γ [8] results. Apart from LNS-GeV-γ, CLAS and CB-ELSA also did not cover the full angular range and had to extrapolate to estimate total
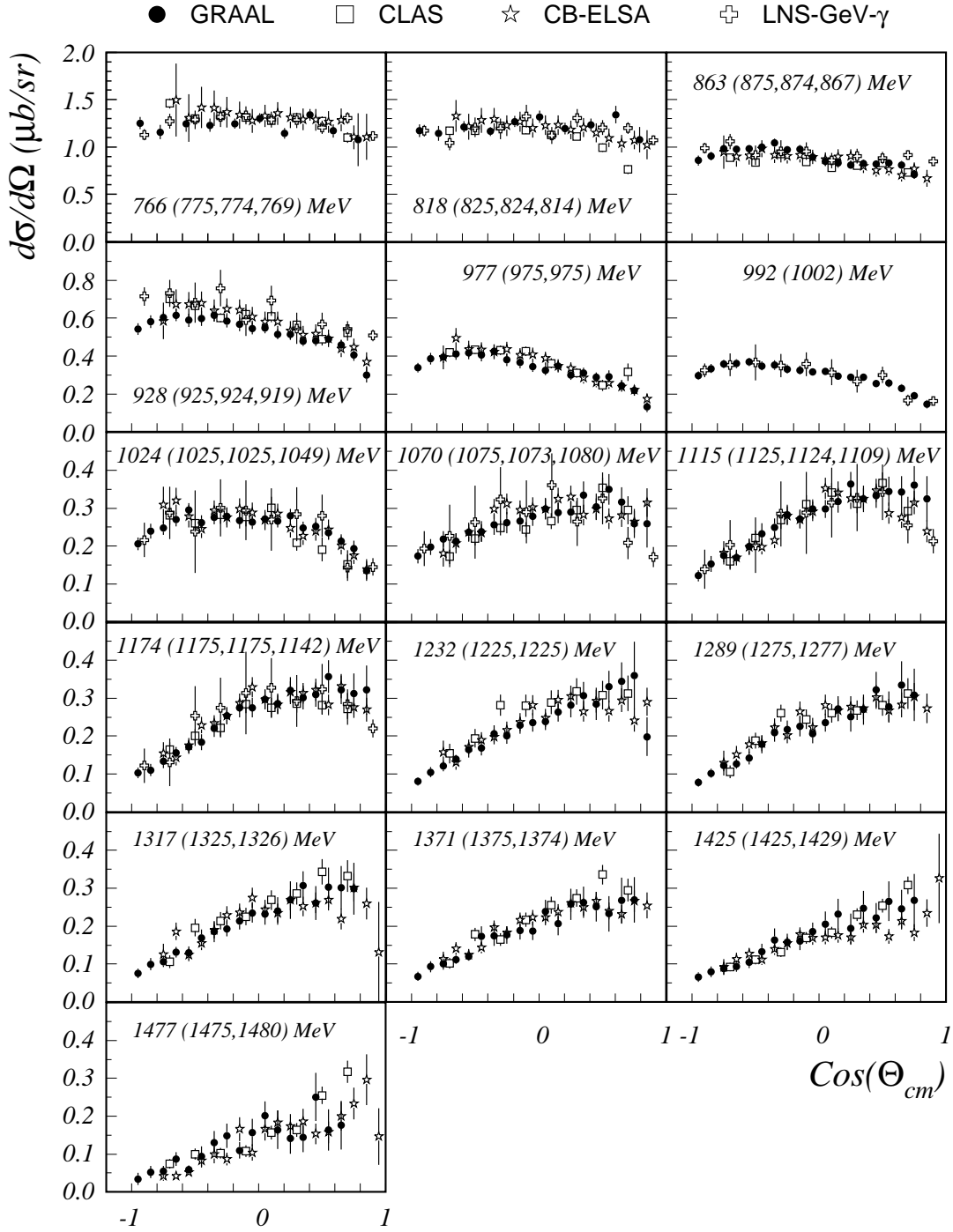
Fig. 11. Comparison between GRAAL (closed circles), CLAS (open squares), CB-ELSA (open stars) and LNS-GeV-γ (open crosses) differential cross-section data for the closest energy bins of the four experiments, from threshold to 1500 MeV (CLAS, CB-ELSA and LNS energy values are in parenthesis).

cross-section. They used MAID and Bonn-Gatchina models, respectively. The new GRAAL estimates agree now well with all other results.

4.5 Discussion

We have compared our results with three models: the isobar model MAID, the coupled-channel partial-wave

analysis developed by the Bonn-Gatchina group and the constituent-quark model of Saghai and Li. In the following, these two latest models will be referred as BCC and CQM, respectively.

The MAID model [12] is an isobar model designed to fit the η photo- and electroproduction database. This model contains, besides Born terms and vector meson exchanges, contributions from the following well-established
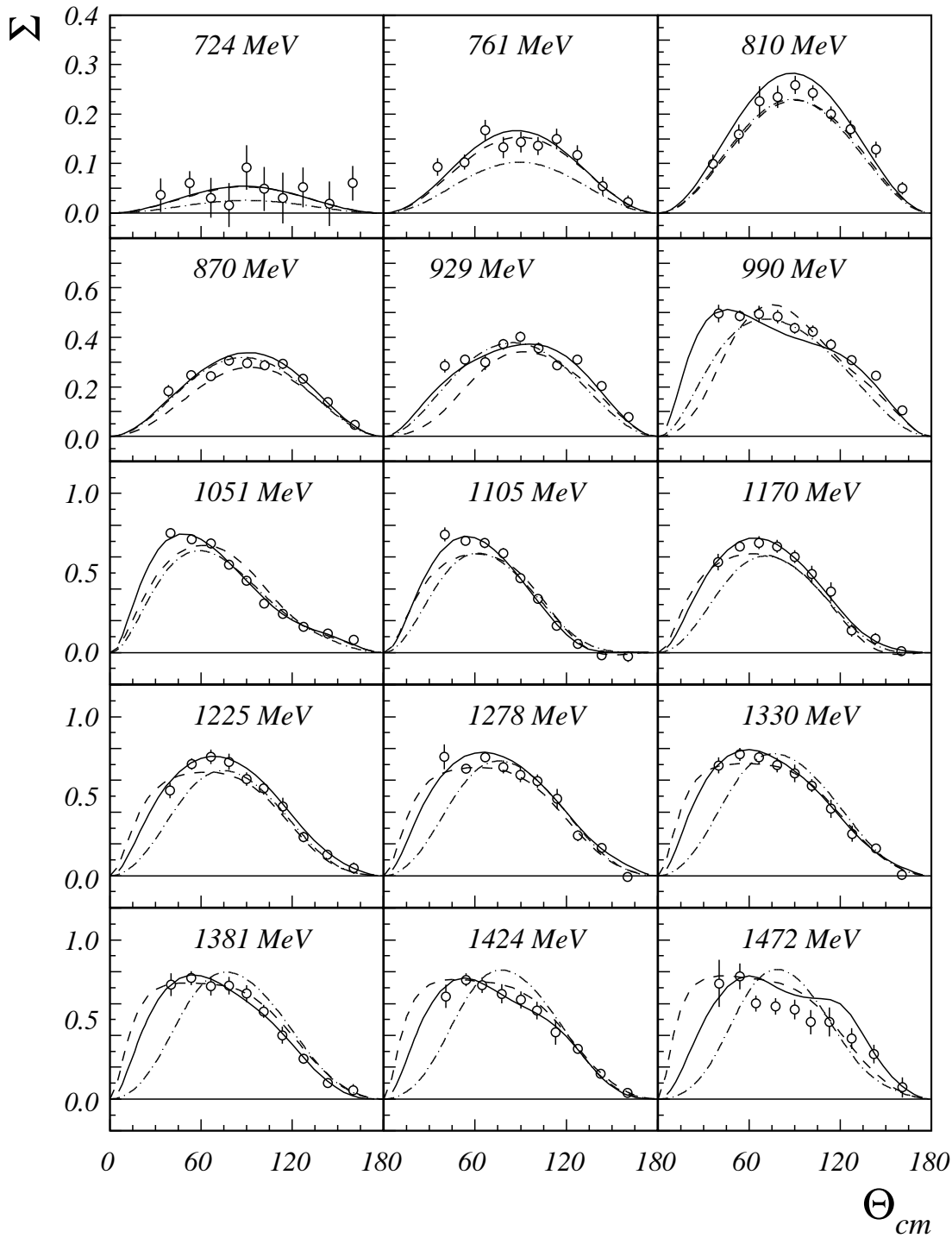
Fig. 12. Angular distributions of the beam asymmetry. Data are compared with results of the MAID (dashed line), CQM (dot-dashed line) and BCC (solid line) models.

resonances: $D_{13}(1520)$, $S_{11}(1535)$, $S_{11}(1650)$, $D_{15}(1675)$, $F_{15}(1680)$, $D_{13}(1700)$, $P_{11}(1710)$ and $P_{13}(1720)$. The model is fitted to current photoproduction cross-section data from Mainz-TAPS [1], GRAAL [4] and CLAS [6] as well as beam asymmetries from GRAAL [2]. The fit gives resonance masses and widths in good agreement with the PDG compilation [22].

In an alternative MAID analysis, the standard treatment of t-channel vector meson exchange is replaced by Regge trajectories while keeping the same N^* contributions [13]. The reggeized version of the MAID model is dedicated to fit the η and η' photoproduction database. Both standard and reggeized models give an overall good description of the current η photoproduction results in the
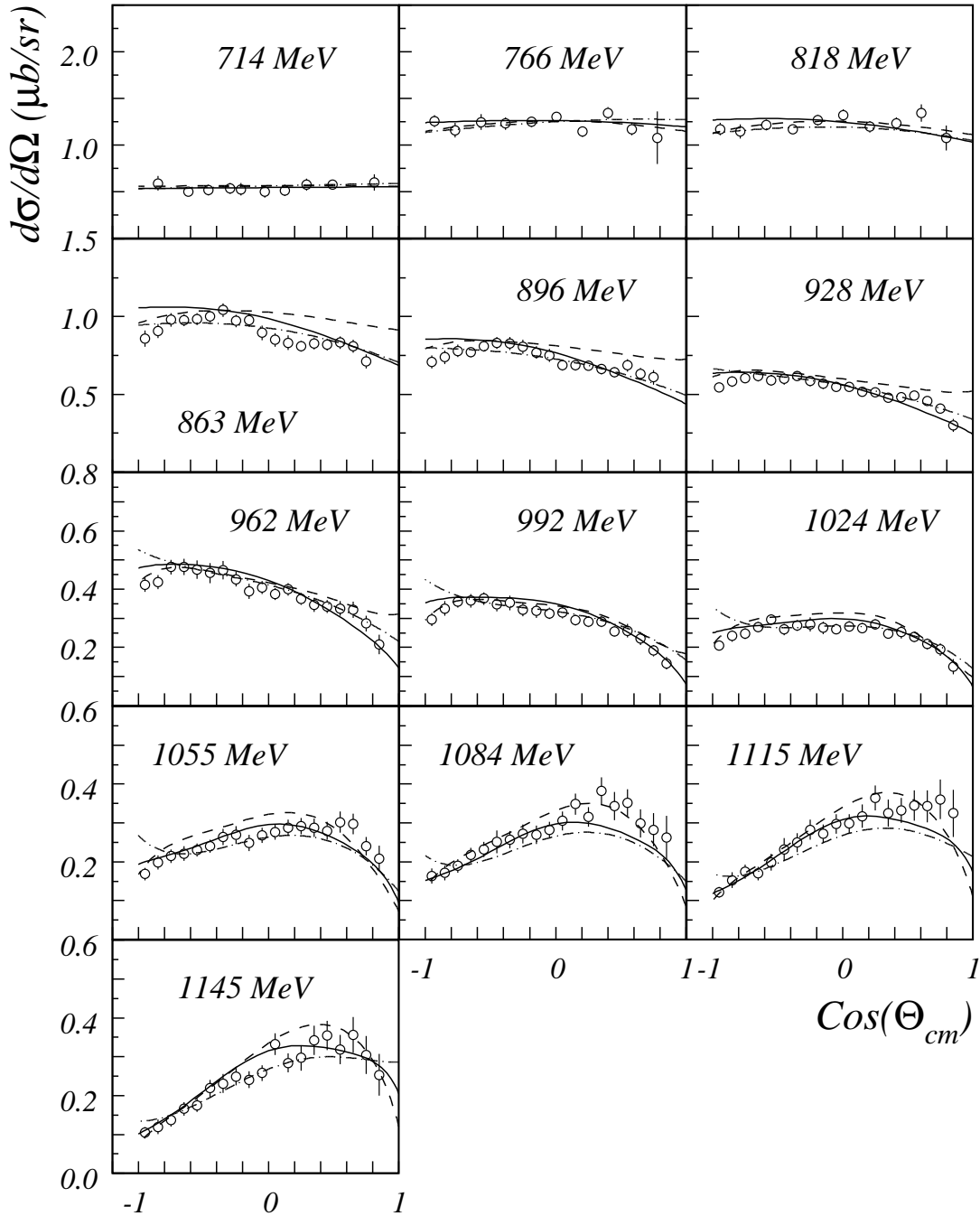
Fig. 13. Differential cross-section for energies ranging from threshold to 1150 MeV. Curve definition as in fig. 12.

resonance region ($W \leq 2$ GeV), the reggeized model becoming more appropriate to describe higher energy data. It was however found that the standard isobar model leads to an unusually large ηN branching ratio (17%) for the $D_{15}(1675)$ resonance, whereas the reggeized model requires a rather small coupling (0.7%) [14].

The BCC model [15,16] is a combined analysis of photoproduction experiments with πN, ηN, $K\Lambda$ and $K\Sigma$ final states. π^0 and η photoproduction data from CB-ELSA [7, 23], Mainz-TAPS [1] and GRAAL [2,17] as well as re-

sults on $\gamma p \rightarrow n\pi^+$ [24] were used. Data available from SAPHIR [25], CLAS [26] and LEPS [27,28] for the reactions $\gamma p \rightarrow K^+\Lambda$, $\gamma p \rightarrow K^+\Sigma^0$ and $\gamma p \rightarrow K^0\Sigma^+$ were also included. As compared to the other models, the BCC partial-wave analysis takes into account a much larger database. A fair agreement with the whole database was obtained with 14 N^* and 7 Δ^* resonances whose masses, widths and electromagnetic amplitudes are compatible with the PDG compilation [22]. One of the main outcome of this model is the necessity to introduce several new res-
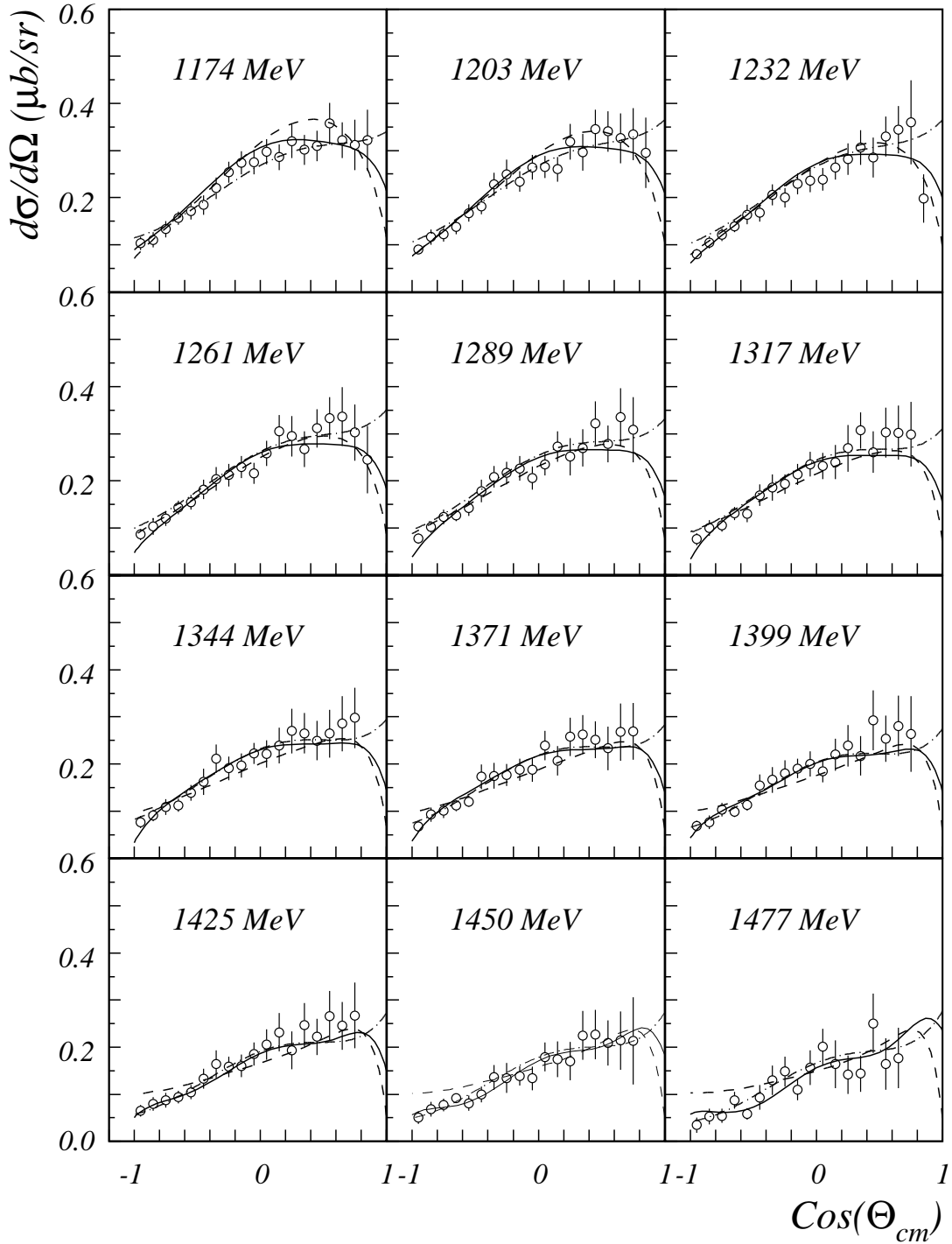
Fig. 14. Differential cross-section for energies ranging from 1150 to 1500 MeV. Curve definition as in fig. 12.

onances above 1800 MeV, in particular the $D_{13}(1875)$ and $D_{15}(2070)$ nucleonic states. The $D_{15}(2070)$ resonance is found to have a sizeable coupling to the ηN final state while the $D_{13}(1875)$ does not significantly contribute. On the other hand, this latter is found to have larger couplings to the $K\Lambda$ and $K\Sigma$ final states as confirmed by our recently published results on $K\Lambda$ and $K\Sigma^0$ photoproduction [19].

The results of the standard MAID [29] and BCC [15] models presented in figs. 3 and 12 to 14 include in their respective database our previously published data up to 1100 MeV and some preliminary beam asymmetry values above 1100 MeV. These two models were not re-fitted to take into account our final data set. For both observables, the overall agreement with the MAID model (dashed line) is quite satisfactory. For the BCC model

(solid line), the agreement is also very good and even better for the beam asymmetry. However, contributions of individual resonances other than the dominant $S_{11}(1535)$ (as well as $S_{11}(1650)$) differ for both models. The fit with the MAID model indeed requires a strong contribution from the $P_{11}(1710)$ partial wave whereas the BCC model needs a strong $P_{13}(1720)$ state (the $P_{11}(1710)$ plays no role). By contrast, the $D_{15}(1675)$ resonance is negligible in the BCC analysis while it has a sizeable contribution in the MAID model.

The CQM model [10,11] is a chiral constituent-quark model and embodies all known nucleonic resonances (the same as in MAID plus $P_{13}(1900)$ and $F_{15}(2000)$). The fitted database contains differential cross-sections and beam asymmetries from Mainz-TAPS [1], GRAAL [2,4], CLAS [6] and CB-ELSA [7,23] up to 2 GeV. Despite the presence of all known resonances, the model could not fit properly our previously published set of data. Only the introduction of a new S_{11}-resonance allowed to reproduce nicely the experimental data [4]. According to the authors, this resonance, not predicted by the Constituent Quark Model, may have an exotic nature such as a ΣK or ΛK molecular state.

The inclusion of our new data in the CQM model has started only recently and the conclusions are still preliminary. Nevertheless, the new fit (dot-dashed line in figs. 12 to 14) confirms the necessity of a third S_{11}-resonance with a mass of 1730 MeV and a width of 240 MeV [30]. It needs also the presence of the two new resonances $D_{13}(1875)$ and $D_{15}(2070)$ with masses and widths in agreement with the predictions of the Bonn-Gatchina model.

Recent experimental and theoretical works in connection to the search for narrow exotic states have focused the attention on η photoproduction on both proton and neutron in the energy region around 1 GeV. Preliminary cross-section data on quasi-free neutron have been recently obtained by the GRAAL [31], CB-ELSA/TAPS [32] and LNS-GeV-γ [33] Collaborations. These results exhibit, in addition to the dominant $S_{11}(1535)$, a resonant structure around $E_\gamma = 1$ GeV ($W = 1.67$ GeV), not seen on the proton to date. Beam asymmetries on quasi-free neutron have also been measured by our Collaboration and will be presented and discussed in a forthcoming article [34]. Several theoretical works have been recently performed to provide an explanation of the structure seen in the cross-section in terms of a baryon resonance predominantly coupled to the neutron. In the framework of the standard MAID model, this bump could be assigned to the $D_{15}(1675)$-resonance [14]. The coupled-channel Giessen model shows that this peak could be interpreted by the $S_{11}(1650)$ and $P_{11}(1710)$ excitations [35]. By contrast, a modified version of the reggeized MAID model shows that the inclusion of an additional exotic narrow $P_{11}(1670)$ state, with a width of 10–30 MeV, could explain the observed structure [36]. This resonance was suggested in some previous works [37–39] to be the nucleon-like member of the anti-decuplet of pentaquarks predicted by the chiral soliton model [40]. The modified reggeized MAID calculation predicts that this state, although much less coupled to the

proton, should also be visible in η photoproduction on the proton. A pronounced narrow structure should be seen mainly at backward angles in the differential cross-section and at all angles in the beam asymmetry [36].

In order to look for this narrow structure, we extracted the differential cross-section and beam asymmetry with the finest energy binning compatible with the energy resolution ($\Delta E_\gamma \sim 16$ MeV). The results obtained between 950 and 1100 MeV are presented in figs. 9 and 10 for various η center-of-mass angles ranging from 40° to 160°. Neither the differential cross-section nor the beam asymmetry do show any evidence of a narrow structure. From the differential cross-section and beam asymmetry results extracted for each of the different data-taking periods, it was checked that no robust narrow signal was hidden or smeared by the data merging. The standard MAID and BCC models remain in fair agreement with our data even with the finer energy binning. In addition, the predictions [36,41] of modified versions of the reggeized MAID model, including a narrow $P_{11}(1670)$ state (10 MeV width), exhibit structures incompatible with our data.

5 Summary

In this paper, we have presented high-precision measurements of the differential cross-section and beam asymmetry for the $\gamma p \to \eta p$ reaction, from threshold to 1500 MeV. The results are in good agreement with all previously published data. For this channel, an extensive database containing accurate beam asymmetries together with differential cross-sections is now available. Various models are able to nicely fit these results but, despite constraints brought by the beam asymmetry, their conclusions remain different in terms of individual resonance contributions. New measurements on other polarization observables are therefore necessary to resolve these ambiguities. The possible contribution of a narrow state $N(1670)$ was also investigated and no evidence was found.

References

1. B. Krusche *et al.*, Phys. Rev. Lett. **74**, 3736 (1995).
2. J. Ajaka *et al.*, Phys. Rev. Lett. **81**, 1797 (1998).
3. A. Bock *et al.*, Phys. Rev. Lett. **81**, 534 (1998).
4. F. Renard *et al.*, Phys. Lett. B **528**, 215 (2002).
5. J. Ahrens *et al.*, Eur. Phys. J. A **17**, 241 (2003).
6. M. Dugger *et al.*, Phys. Rev. Lett. **89**, 222002 (2005).
7. V. Credé *et al.*, Phys. Rev. Lett. **94**, 012004 (2005).
8. T. Nakabayashi *et al.*, Phys. Rev. C **74**, 035202 (2006).
9. D. Elsner *et al.*, arXiv:nucl-ex/0702032.

10. Z. Li, B. Saghai, Nucl. Phys. A **644**, 345 (1998).
11. B. Saghai, Z. Li, Eur. Phys. J. A **11**, 217 (2001); B. Saghai, Z. Li, *Proceedings of the NSTAR2002 Workshop on the Physics of Excited Nucleons, Pittsburgh, 2002*, edited by S.A. Dytman, E.S. Swanson (World Scientific, 2003) arXiv.nucl-th/0305004.
12. W.-T. Chiang, S.N. Yang, L. Tiator, D. Drechsel, Nucl. Phys. A **700**, 429 (2002).
13. W.-T. Chiang, S.N. Yang, L. Tiator, M. Vanderhaeghen, D. Drechsel, Phys. Rev. C **68**, 045202 (2003).
14. L. Tiator, *Proceedings of the Meson2006 Workshop, Cracow, 2006*, Int. J. Mod. Phys. A **22**, 297 (2007) arXiv:nucl-th/0610114.
15. A.V. Anisovich *et al.*, Eur. Phys. J. A **25**, 427 (2005).
16. A.V. Sarantsev *et al.*, Eur. Phys. J. A **25**, 441 (2005).
17. O. Bartalini *et al.*, Eur. Phys. J. A **26**, 399 (2005).
18. V.G. Gurzadyan *et al.*, Mod. Phys. Lett. A **20**, 19 (2005).
19. A. Lleres *et al.*, Eur. Phys. J. A **31**, 79 (2007).
20. F. Renard, Thesis, University J. Fourier (Grenoble) 1999, unpublished.
21. L. Mazzaschi *et al.*, Nucl. Instrum. Methods A **436**, 441 (1994).
22. Review of Particle Physics 2004, Phys. Lett. B **592**, 1 (2004).
23. O. Bartholomy *et al.*, Phys. Rev. Lett. **94**, 012003 (2005).
24. K.H. Althoff *et al.*, Phys. Rev. C **18**, 199 (1983); K. Buechler *et al.*, Nucl. Phys. A **570**, 580 (1994).
25. K.-H. Glander *et al.*, Eur. Phys. J. A **19**, 251 (2004).
26. J.W.C. McNabb *et al.*, Phys. Rev. C **69**, 042201(R) (2004).
27. R.G.T. Zegers *et al.*, Phys. Rev. Lett. **91**, 092001 (2003).
28. R. Lawall *et al.*, Eur. Phys. J. A **24**, 275 (2005).
29. W.-T. Chiang, C. Bennhold, L. Tiator, *ETA-MAID2003 isobar model with single poles for vector meson exchange*; results available at the website www.kph.uni-mainz.de/MAID/eta2003.
30. B. Saghai, private communication.
31. D. Rebreyend *et al.*, *Proceedings of the 10th International Symposium on Meson-Nucleon Physics and the Structure of the Nucleon, Beijing, 2004*, Int. J. Mod. Phys. A **20**, 1554 (2005) nucl-ex/0411025; V. Kuznetsov *et al.*, *Proceedings of the NSTAR2004 Workshop on the Physics of Excited Nucleons, Grenoble, 2004* (World Scientific, Singapore, 2004). Preliminary GRAAL integrated cross-sections show that, contrary to the CB-ELSA/TAPS results, the σ_n/σ_p ratio remains greater than 1 above 1 GeV.
32. I. Jaegle *et al.*, *Proceedings of the NSTAR 2005 Workshop on the Physics of Excited Nucleons, Tallahassee, 2005*, edited by S. Capstick, V. Crede, P. Eugenio (World Scientific, Singapore, 2006); B. Krusche *et al.*, *Proceedings of the 4th International Conference on Quarks and Nuclear Physics, Madrid, 2006*, Eur. Phys. J. A **31**, 485 (2007).
33. J. Kasagi, Talk at the *Yukawa International Seminar YKIS2006, Kyoto, 2006*, http://www2.yukawa.kyoto-u.ac.jp/~ykis06/.
34. A. Fantini *et al.*, submitted to Phys. Rev. C.
35. V. Shklyar, H. Lenske, U. Mosel, arXiv.nucl-th/0611036 (2006).
36. A. Fix, L. Tiator, M.V. Polyakov, arXiv.nucl-th/0702034 (2007).
37. M.V. Polyakov, A. Rathke, Eur. Phys. J. A **18**, 691 (2003).
38. R.A. Arndt, Y.I. Azimov, M.V. Polyakov, I.I. Strakovsky, R.L. Workman, Phys. Rev. C **69**, 035208 (2004).
39. D. Diakonov, V. Petrov, Phys. Rev. D **69**, 094011 (2004).
40. D. Diakonov, V. Petrov, M. Polyakov, Z. Phys. A **359**, 305 (1997).
41. L. Tiator, private communication.